MATEC Web of Conferences **383**, 00012 (2023) https://doi.org/10.1051/matecconf/202338300012
Power System Engineering 2023

Effect of sharp/oblate nose on a model subsonic rocket measured by PIV

Filip Klátil[1*], *Jiří* Brtník[1], *Jan* Peprný[1] and *Martin* Suchý[1]

[1]University of West Bohemia in Pilsen, Univerzitní 22, Pilsen, 306 14, Czech Republic

Abstract. What is the difference between the wake past a rocket with sharp nose or with oblate nose? The measurement by Particle Image Velocimetry tries to answer at velocities 5 – 20 m/s (i.e. Reynolds numbers 20 thousand to 79 thousand). A simple model rocket is 3D printed with body diameter of 60 mm, total height 4 D, i.e. 240 mm. The maps of mean stream-wise velocity, stream-wise fluctuations and span-wise fluctuations are compared.

1 Introduction

In the movie The Dictator [1], there is a scene, when the dictator visits a research center asking about progress in rockets. He sees the rocket with an oblate round nose and complains, that the nose has to be sharp to scare the enemies. The scientist tries to explain him, that it is not important at the current stage. But dictator is a dictator.

In this conference contribution, we asked ourselves the question, what is the difference between sharp and oblate nose on a rocket? Answering this question by using experimental approach has been a topic of a seminar work for group of four students (authors of this contribution). The awesome equipment of the University of West Bohemia has been used to perform a simple wind tunnel experiment to compare both possibilities. This contribution is based on the student seminar work; thus the first goal was to obtain the credit (zápočet). Therefore, we please You, dear reader or reviewer, for leniency with this work.

1.1 Literature

Easanesan et al [2] used PIV (Particle Image Velocimetry, [3]) to explore the effect of nose shape to the wake past a body. The body was a prismatic rectangular cylinder. The two compared noses were the elliptical nose and the nose from "Ahmed body" [4]. Additionally, the work [2] discusses the effect of the proximity to the ground. They found, that the importance of the nose shape increases in the presence of the ground.

Velmani and Suresh [5] used advanced numerical simulation to compare the supersonic flow around two noses: the parabolic nose and the spherically blunted nose (i.e. cone with relatively large radius at the tip). In addition, they varied the turbulence intensity of the incoming flow from 5 % to 20 %. They did not observe severe influence of the incoming

* Corresponding author: klatilf@students.zcu.cz

turbulence to the topology of the flow. On the other hand, the nose shape has large impact on the topology of shock waves and their sharpness.

Bountin et al. [6] investigated the transition to turbulence on the surface of a nose with very sharp or blunted tip in terms of thermal boundary layer and static pressure oscillations in several locations downwards on the cone surface. Additionally, they play with the nose tip heating or cooling.

A very practical engineering question has been solved by Chen et al. [7]. The measured and computed the pressure distribution on a wall of tunnel, where meet two fast trains. The measurement was performed with a real Chinese train CRH6A with nose length 4 m. The computation with increased nose length up to 12 m shows, that increasing nose length decreases the pressure pulse, the maximum drag and the side force pulse during the meeting.

Duda and Uruba [8] investigated the flow separation around a sudden step in a wind tunnel. They found, that the real occurrence of fluctuation coherent structures exceeds the shear layer. The separation bubble is formed, but the velocity at its boundary is zero only in average sense, the instantaneous velocities show rich and wild flow. To separate the flow structures, authors suggest the Agrawal [9] (spatial) decomposition instead of Reynolds (temporal) decomposition.

2 Experimental setup

The experiment is held in the laboratory of flow measurement at the University of West Bohemia in Pilsen [10]. This laboratory is equipped by excellent scientific instruments, which we were allowed to use to our small student experiment.

2.1 Geometry modelling

The beginning of the work was to create 3D model for the rocket nose. There were two types of noses modelled: the ellipsoidal and conical one. The diameter $D = 60$ mm, height H of the cylindrical part is $H = 2 \cdot D = 120$ mm, height of both noses is too H. The first attempt has been performed within the CAD/CAM software SolidWorks (see Fig. 1 left). Here created model has been exported into the Blender software used to smoothing of the model and exporting into the *stl* format suitable for 3D printer.

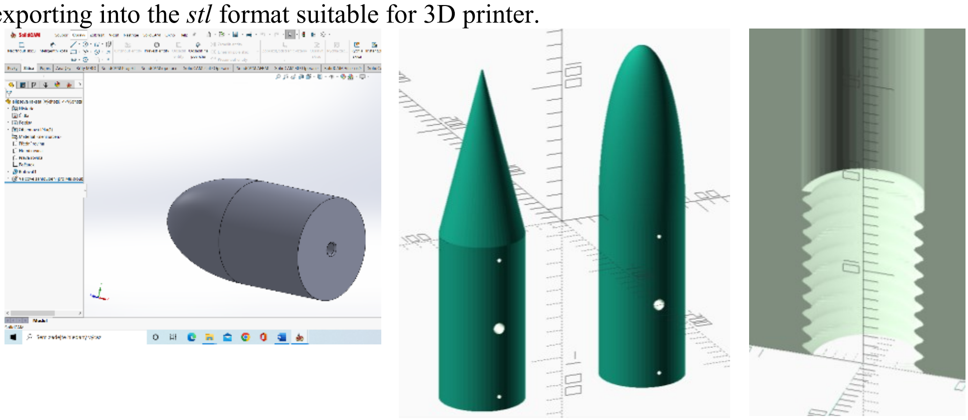

Fig. 1. Left: the model creation within the SolidWorks. **Middle**: the model rockets (body + nose) prepared in OpenSCAD. **Right**: detail view to the screw hole for connecting rocket body with the noses; modelled in OpenSCAD.

However, it has been decided to made the model of two parts: the cylindrical body and the nose, which has would be replaceable and to connect these parts by a screw M12.

Additional task was to model three holes into the body perpendicular to the axis of the body cylinder in order to fix the model to the ceiling of the wind tunnel (bigger hole of diameter 10 mm) and to fix its orientation (smaller hoes of diameter 3 mm). The complexity of the model even arose, when our supervisor noticed, that the infinitely sharp edge of the conical nose would not be printable in a repeatable way and he recommended to make it with a radius. With all the mentioned details the task started to be too complicated for both Blender and SolidWorks. The final model has been created by using the OpenSCAD program with help of our supervisor; see Fig. 1 middle. The conical nose has been created as a convex hull of sphere of diameter 1.2 mm at the top and a thin disk at the base. The oblate nose is modelled as a sphere of diameter D and elongated 4× along the axial coordinate, one half removed out. The hole for screw is modelled as a twisted linear extrude of eccentric circle. The inner diameter is 10.2 mm, the outer it 12.0 mm, the thread pitch is 1.75 mm.

2.2 3D print

The components were printed by using the commercial 3D printer Prusa Mk 2.5 from the polymerized lactic acid PLA [11]. There was 3 parts printed: the cylindrical body, the oblate nose and the conical nose.

2.3 Model finishing

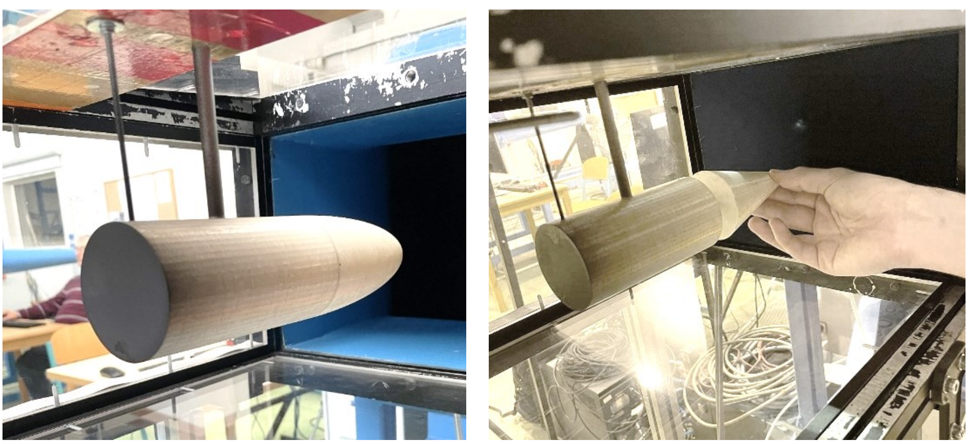

Fig. 2. Model inside the wind tunnel. The back plane is painted to avoid laser reflections during PIV measurements. **Left**: with oblate nose **Middle**: with conical nose.

The 3D printed surface is not smooth enough due to the printing layers. This roughness has been reduced by repeated filling by using fine sand-paper and by covering by a transparent nitro-cellulose lack. Additionally, the back base has been painted by using a spray of butyl-acetate base black lack. The reason is to reduce the reflections of laser during the PIV measurement. Next step was cutting the thread with a tap, as the 3D printed thread is not sufficient for smooth screwing.

2.4 Optical scanning

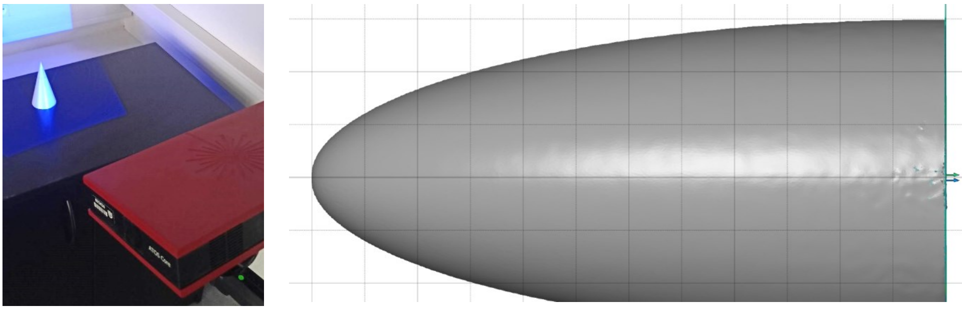

Fig. 3. Scanning of the product. **Left**: photograph of the scanning process **Right**: Scan of the oblate nose.

The 3D optical scanning has been performed by using a system Atos from company GOM. The object is placed into the *measuring volume* and illuminated by a projector (see Fig. 3 left). A *fringe pattern* is projected on the surface [12] and their deformation observed by two cameras from slightly different positions is recalculated to the exact surface position. To increase the accuracy, more scans has to be done and these scans are connected by using small paper targets glued to the scanned object. This system is used in the Pilsen laboratory to specify the precision of boundary conditions in the experiments [13] [14] and to detailed study of the effect of boundary condition inaccuracies [15] [16].

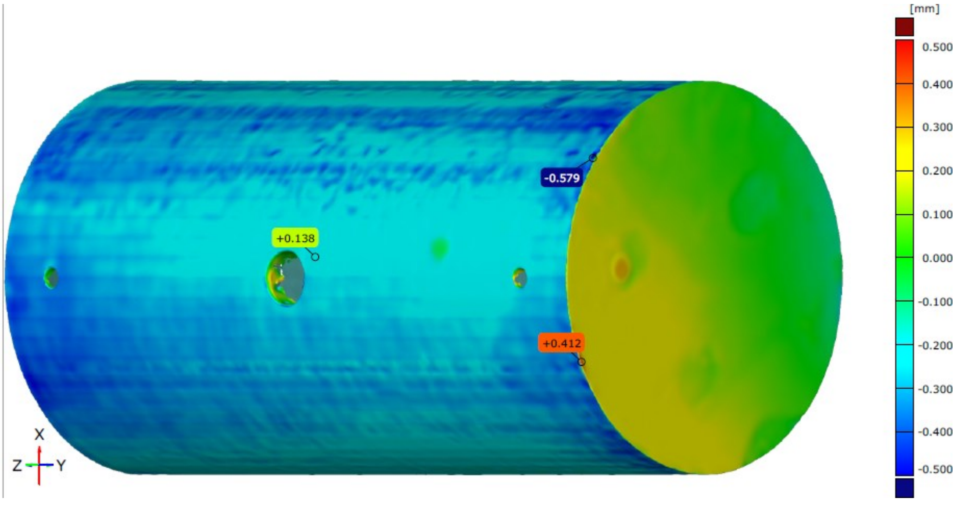

Fig. 4. Spatial distribution of the deviations from nominal (designed) geometry of the body of the rocket model.

The found integral deviations from the nominal geometry are listed in Table 1. These parameters are obtained by using fitting procedure – the scanned data are fitted by cylinder, cone or ellipse and the properties of fitted geometrical shape is compared with the expected value of the CAD model:

2.5 Wind tunnel

University of West Bohemia in Pilsen is equipped by a large open wind tunnel [17] [18] [19] with test section cross-section $0.3 \times 0.2\ m^2$. In publication [18], it is proven, that the tunnel has tough construction and it does not deform significantly under running conditions [20]. The tunnel power is controlled by using pressure sensors to keep the constant velocity. The velocity can be controlled in the range from 2 to 90 m/s. We used only velocities 5, 10 and 20 m/s in our measurement.

Table 1. Properties of nominal geometric shapes and shapes fitted on scanned actual element.

Property	Actual	Nominal
Body diameter [mm]	59.438	60.000
Body height [mm]	120.156	120.000
Distance of connecting rods [mm]	100.123	100.000
Sharp nose angle [°]	13.68	13.85
Oblate nose – larger ellipse diameter [mm]	238.240	240.000
Oblate nose – smaller ellipse diameter [mm]	59.642	60.000

3 Particle Image Velocimetry

The method of Particle Image Velocimetry (PIV) is standard laboratory methods nowadays. It is based on observing small particles carried by the flow [21] under the assumption, that the particles follow the flow [3], which has been proven to work even in very fast and complex flows inside a turbine [22], although the another liquid can make troubles in such a complicated case [23]. The output of the PIV method is a two-dimensional velocity vector field. These vectors can be three-dimensional [24] in case of using a pair of cameras. The more simple case used in this study uses one camera only and produces a field of two-dimensional vectors, where the third dimension can be statistically represented, if some assumptions about isotropy are fulfilled [13], or it is safer to just omit it than manipulate the data. The motion of the particles is captured by using two consecutive pulses of the illuminating solid-state laser, but these snapshots are separated by a time, which is long in the scale of studied flow. However, there exist fast systems as well [25] [26], but the Pilsen laboratory is equipped by the "slow" system only. The fast system is suitable for the tracking Lagrangean study of quantum turbulence in superfluid helium [27] [28], which has been already used to discover the similarity in oscillatory secondary flows [29], the oscillatory wake flows [30] and cavitation [31] and mainly the discovery, that the quantum and classical turbulence is universal in dependence to the probed length-scale [32]. The effect, which is not universal, is the thermal convection [33]. PIV is best for studying the key component of turbulence – vortices. To do this, our amazing supervisor developed algorithm for their detection [34] and discovered a new vortex profile [35].

3.1 Calibration

The PIV system needs to be calibrated. We used a special calibration ruler of our supervisor. This ruler was placed behind trailing plane of the rocket horizontally into the height of the maximum diameter of the rocket, i.e. that the rocket axis lies in the plane of the ruler. The correct height has been reached by placing the ruler on a column of cups from coffee drunk by our supervisor. Then the camera was focused into the plane of the ruler. The focusing has been checked on the monitor of computer. When the supervisor was satisfied, single snapshot has been captured and saved for the calibration. The calibration measures the relation between the physical distance in millimeters and the image distance represented by pixels. To do this, the function "Measure Scale Factor" in the software "Dantec Dynamic

Studio" has been used. The Scale Factor is 9.313, therefore one interrogation area (IA) has size 2.205 mm.

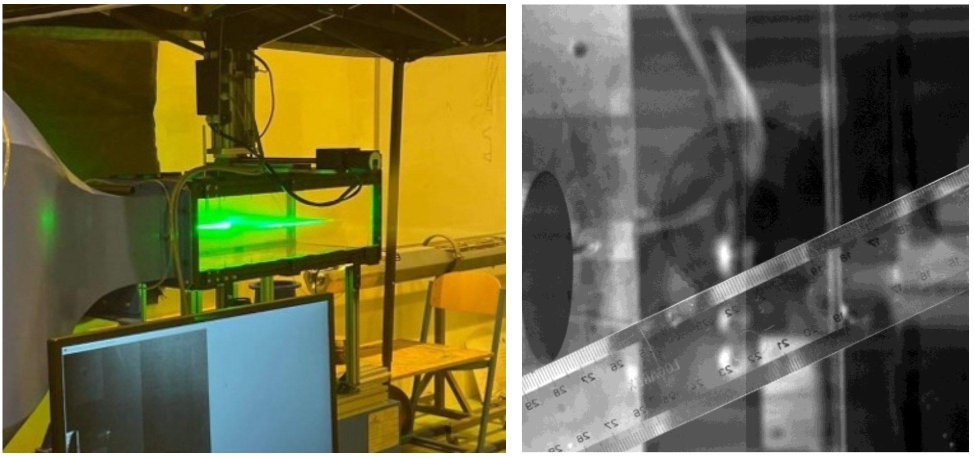

Fig. 5. PIV calibration and measurement. **Left**: photograph of the PIV measuring process **Right**: Calibration photograph.

Second step was to fit the plane of the laser sheet to the plane of the ruler. This was achieved by switching on the laser for a minimum power and rotating a pair of screw rods to move the laser head up or down as needed. In the correct position, the ruler was illuminated only from side visualizing small dust particles on the ruler surface by side illumination. During this procedure, the camera has been covered to avoid random reflection from the ruler, which could damage the chip.

Third step was to remove the calibration ruler, run the wind tunnel, put the particles of the fog and try to measure the motion. The particles were illuminated well, their images were sharp and thus our supervisor concluded, that we can continue to the measurement.

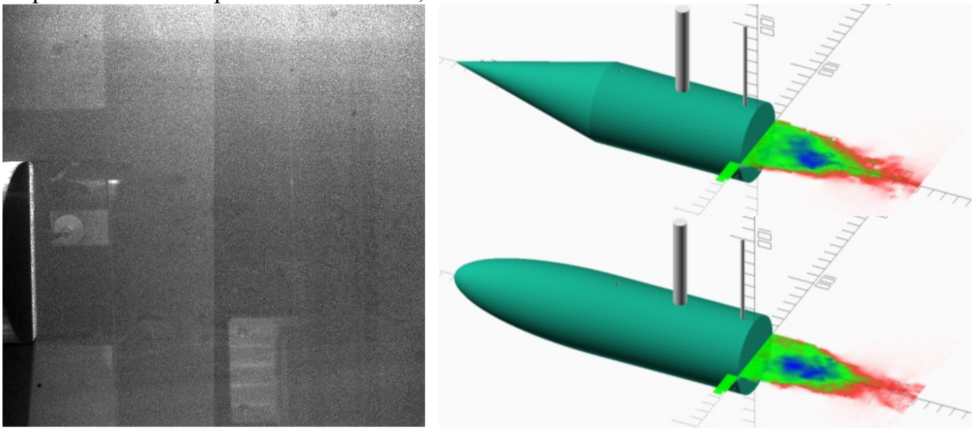

Fig. 6. PIV measurement. **Left**: single PIV snapshot at 5 m/s with oblate nose. The rocket body is on the left hand side of the photograph. Under the body, there is a shadow. The velocities measured in the shadow are all zero. The other visible objects are outside of the transparent wind tunnel test section. **Right**: Visualization of single instantaneous field of stream-wise velocity component u by using the software OpenSCAD. Top subpanel shows the sharp nose, while the bottom one the oblate nose.

3.2 PIV measurement

The measurement consisted of two pulses of the laser separated by a relatively short time ΔT. The droplets of Safex fog moved during this period by a small distance. By the knowledge of scale factor and the time ΔT between pulses, the function "Adaptive PIV" calculates the average velocity in each interrogation area from the shift of crosscorrelation peak between the two photographs separated by the time ΔT. The average translated distance has to be divided by the time ΔT to get the velocity in meters per second. This is an average velocity across the interrogation area (i.e. in a volume 2.205 × 2.205 × ~1 mm^3, where the last is the thickness of the laser sheet) and during the time between pulses ΔT. Table 2 contains the names, times, velocities, ΔTs, Reynolds number based on rocket body diameter and the nose type for each captured dataset.

Table 2. Properties captured datasets.

Dataset name	**Time** [hh:mm:ss]	***U*** [m/s]	**ΔT** [s]	**Re** [1]	**Nose**
Run 16:08:53-Bt-5ms	16:08:53	5	$2 \cdot 10^{-4}$	$1.98 \cdot 10^{4}$	Oblate
Run 16:25:46-Bt-10ms	16:25:46	10	$1 \cdot 10^{-4}$	$3.96 \cdot 10^{4}$	Oblate
Run 16:44:29-Bt-20ms	16:44:29	20	$5 \cdot 10^{-5}$	$7.92 \cdot 10^{4}$	Oblate
Run 17:22:33-At-5ms	17:22:33	5	$2 \cdot 10^{-4}$	$1.98 \cdot 10^{4}$	Sharp
Run 17:38:54-At-10ms	17:38:54	10	$1 \cdot 10^{-4}$	$3.96 \cdot 10^{4}$	Sharp
Run 17:59:42-At-20ms-b	17:59:42	20	$5 \cdot 10^{-5}$	$7.92 \cdot 10^{4}$	Sharp

4 Results

4.1 Reynolds number $1.98 \cdot 10^4$

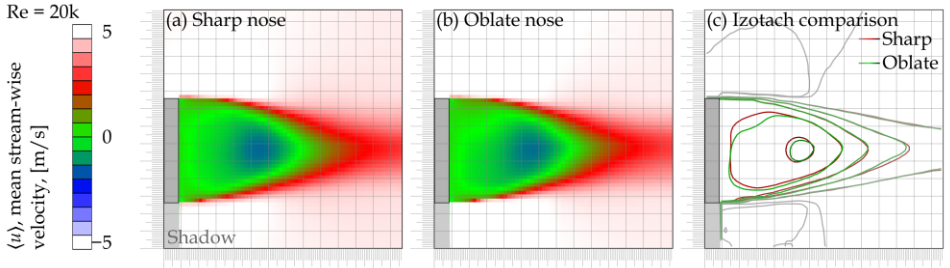

Fig. 7. Comparison of the mean stream-wise velocity u for the both nose types at reference velocity 5 m/s, i.e. diameter-based Reynolds number $1.98 \cdot 10^4$.

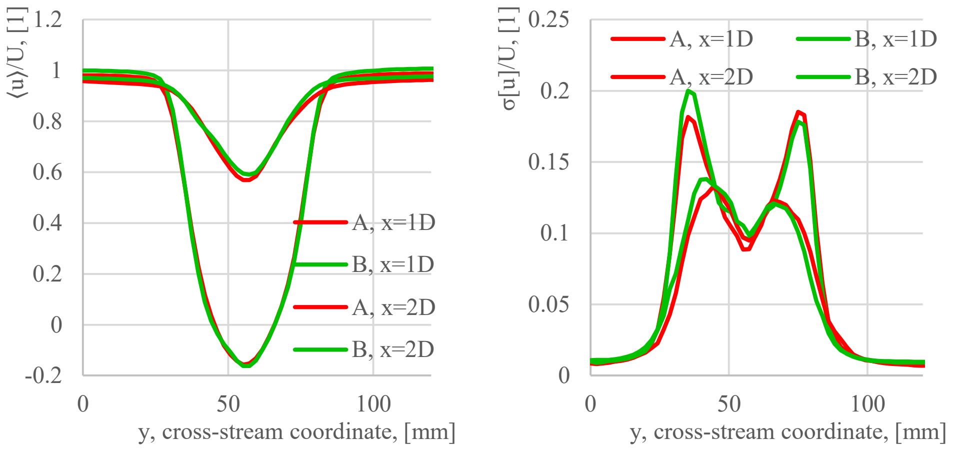

Fig. 8. Cross-sectional profile of the mean stream-wise velocity u (left) and for its standard deviation (right) for the both nose types at reference velocity 5 m/s, i.e. diameter-based Reynolds number $1.98 \cdot 10^4$. The full colors represent the section in stream-wise distance 60 mm i.e. $1 \cdot D$ past the rocket, while the lighter colors play for distance $2 \cdot D$.

The mean velocity is displayed in Fig. 1. It is calculated as an ensemble average of instantaneous velocities measured in each interrogation area of the observed image:

$$\langle u\rangle(x,y) = \frac{1}{N}\sum_{i=1}^{N} u(x,y,t_i) \tag{1}$$

The fluctuations $\sigma[u]$ are calculated as

$$\sigma[u](x,y) = \left(\frac{1}{N}\sum_{i=1}^{N}\big(u(x,y,t_i) - \langle u\rangle(x,y)\big)^2\right)^{\frac{1}{2}} \tag{2}$$

but our supervisor knows a trick to avoid the need of mean value during the calculation of this and he is able to calculate both, $\langle u\rangle$ and $\sigma[u]$ by a single cycle. The trick is simple, but it needs to be explained twice. In the next, we will use $\langle..\rangle$ instead of general averaging in the form of (1):

$$\begin{aligned} \sigma^2[u] &= \langle (u - \langle u\rangle)^2\rangle = \\ &= \langle u^2 - 2u\langle u\rangle + \langle u\rangle^2\rangle = \\ &= \langle u^2\rangle - \langle 2u\langle u\rangle\rangle + \langle\langle u\rangle^2\rangle \end{aligned} \tag{3a}$$

where he used the binomial equation $(a+b)^2 = a^2 + 2ab + b^2$. Next part is, that average value behaves as a constant in respect to averaging. Therefore $\langle 2u\langle u\rangle\rangle = 2\langle u\rangle\langle u\rangle = 2\langle u\rangle^2$ and double averaging is just simple averaging. Then

$$\sigma^2[u] = \cdots = \langle u^2\rangle - \langle u\rangle^2 \tag{3b}$$

Therefore, during the summation, it is just needed to count two variables, first for first power – just the sum, a second for the second power, then both divide by the number of snapshots and subtract.

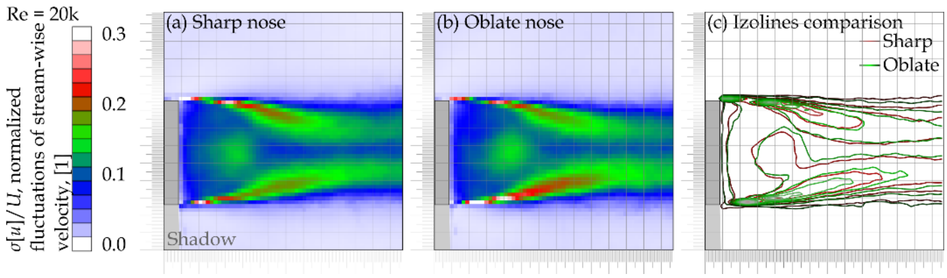

Fig. 9. Comparison of the fluctuations of mean stream-wise velocities $\sigma[u]/U$ for the both nose types at reference velocity 5 m/s, i.e. diameter-based Reynolds number $1.98 \cdot 10^4$.

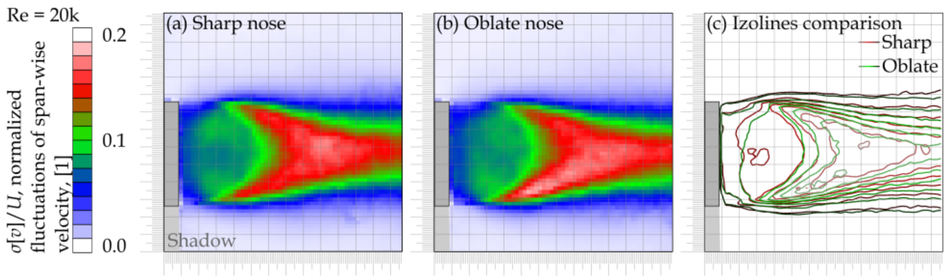

Fig. 10. Comparison of the fluctuations of mean span-wise velocities $\sigma[v]/U$. In contrast to Fig. 9, the legend maximum is lower (0.2 instead of 0.3), and the topology is different: the stream-wise fluctuations are focused in the shear region at the boundary of the young wake, while the span-wise fluctuations dominate the area in the center of the slightly developed wake.

Figures 9 and 10 show the spatial maps of fluctuations in stream-wise and span-wise directions. The stream-wise fluctuations reach maxima at the near shear layer just behind the body. These shear layers continue spreading and move towards the axis, but there is a local minimum at the obstacle axis. On the other hand, the span-wise fluctuations have maximum at the axis and their start is shifted stream-wards into the places, where the von Kármán vortex street start to form [36].

The contrast between fluctuations in these two directions can be quantified in terms of *Degree of Anisotropy* DA [37], [19] defined as

$$DA = \frac{\sigma^2[u] - \sigma^2[v]}{\sigma^2[u] + \sigma^2[v]} \tag{4}$$

Its spatial distribution (Fig. 11 a, d) shows the dominance of span-wise fluctuations at the axis and stream-wise at the boundary of the wake. The spectral decomposition according to length-scale of the fluctuations (Fig. 11 b, c, e, f) shows, that the stream-wise fluctuations are connected with small scales, the small-scale fluctuations in surrounding flow are isotropic. At large-scales, the surrounding flow is dominated by stream-wise fluctuations, which can be caused by the instability of the wind-tunnel control circuit [17]. The area near wake axis is clearly dominated by span-wise fluctuations of the starting von Kármán vortex street [36] [38].

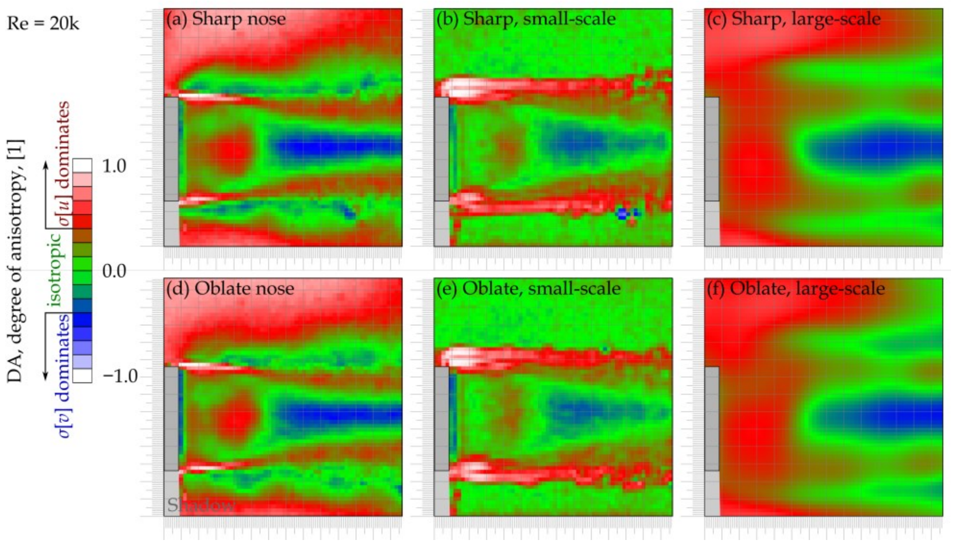

Fig. 11. Degree of anisotropy, see equation (4). Fluctuations in green areas are isotropic, while red areas are dominated by stream-wise fluctuations and blue ones oppositely.

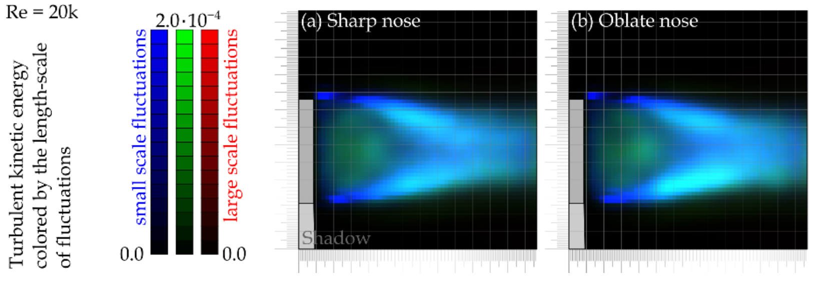

Fig. 12. Turbulent kinetic energy colored by the length-scale of fluctuations causing it [39]. Blue colors correspond to small scale fluctuations (see the pure blue in thin shear layers), green color channel describes the "middle" scales of fluctuations (see the area close behind the end), red colors represent large-scales, which are depleted in this case. The relative amplitude is scaled to the band width and to the Kolmogorov law [40] in a such way, that the ideal homogenous turbulence of Kolmogorov style would be displayed in shades of grey.

The separation of length-scales is performed by algorithm [39] created by our supervisor. It is based on the ideas of Agrawal [9] [41] and Kolmogorov [40]. Please look into the mentioned papers for more information.

4.2 Reynolds number $3.96 \cdot 10^4$

In this section, we present the data at velocity 10 m/s corresponding to Reynolds number $3.96 \cdot 10^4$.

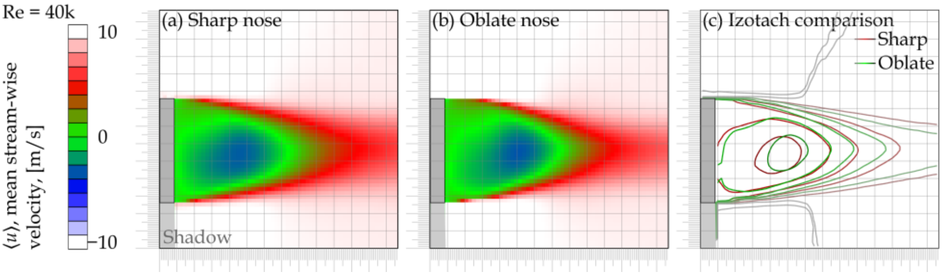

Fig. 13. Mean stream-wise velocity at the velocity 10 m/s corresponding to rocket-diameter-based Reynolds number $3.96 \cdot 10^4$.

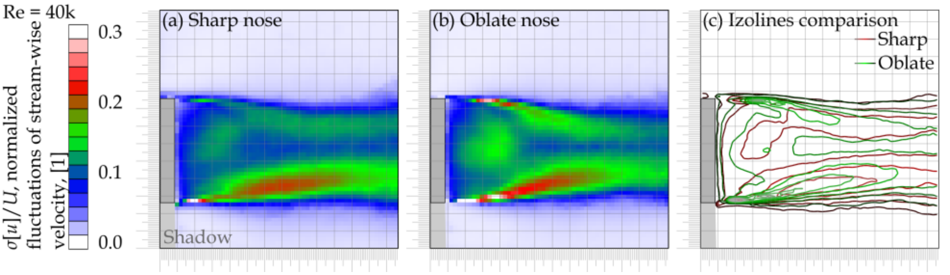

Fig. 14. Stream-wise velocity fluctuations.

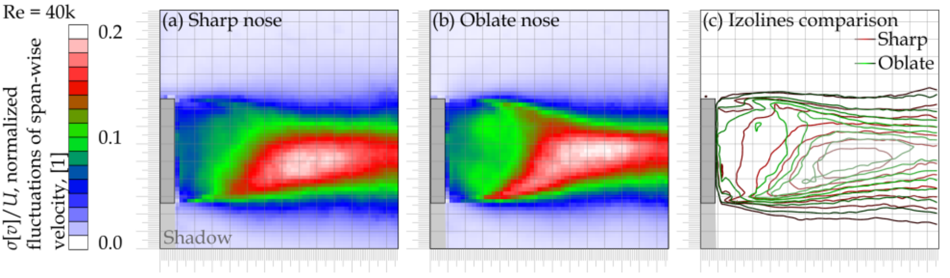

Fig. 15. Span-wise velocity fluctuations.

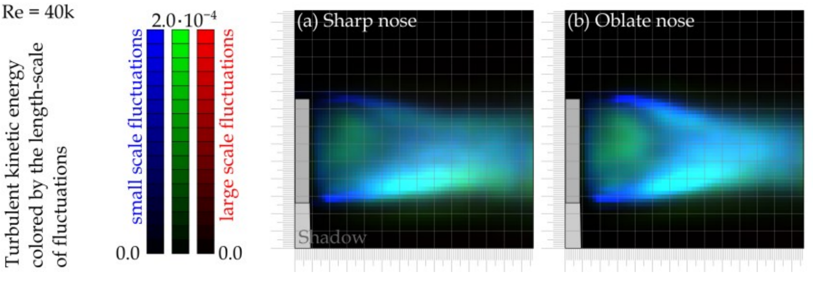

Fig. 16. Turbulent kinetic energy colored by the length-scale of fluctuations. Please read the articles [39] [8] [9] [9] for better understanding. Here, the blue colors represent small-scale fluctuations, green middle-scale and red large-scale.

At the higher velocity, the asymmetry increases between top and bottom side of the wake. The reason is not sure, probably it is caused by wrong montage into the wind tunnel – the model is not placed directly against the flow, although we have checked this issue. Second reason can be the support rods, which influence the boundary layer at the hull. Professor Uruba mentioned, that the flow around rockets can spin. Therefore, the rod influences the result even in a perpendicular plane.

4.3 Reynolds number $7.92 \cdot 10^4$

In this section, we present the data at velocity 20 m/s corresponding to Reynolds number $7.92 \cdot 10^4$.

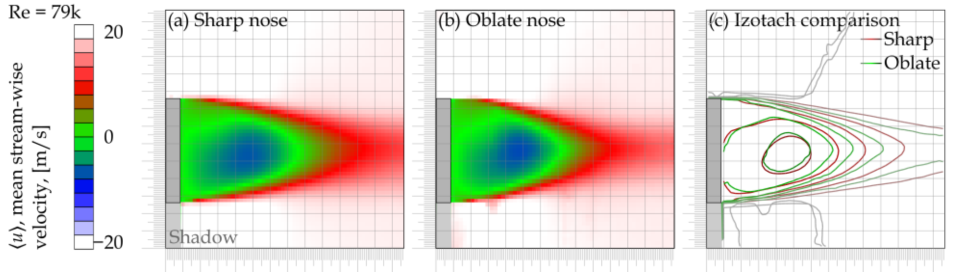

Fig. 17. Mean stream-wise velocity at the velocity 20 m/s corresponding to rocket-diameter-based Reynolds number $7.92 \cdot 10^4$.

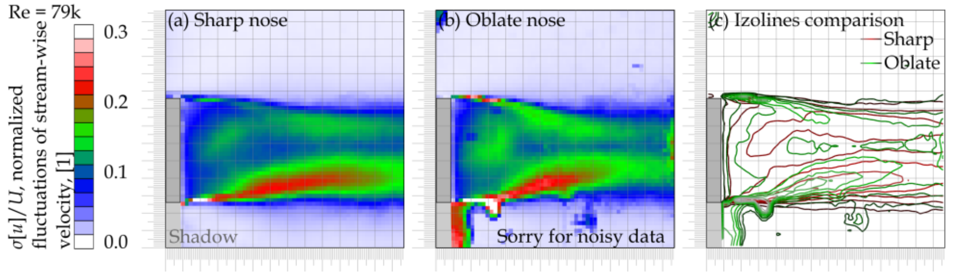

Fig. 18. Stream-wise velocity fluctuations.

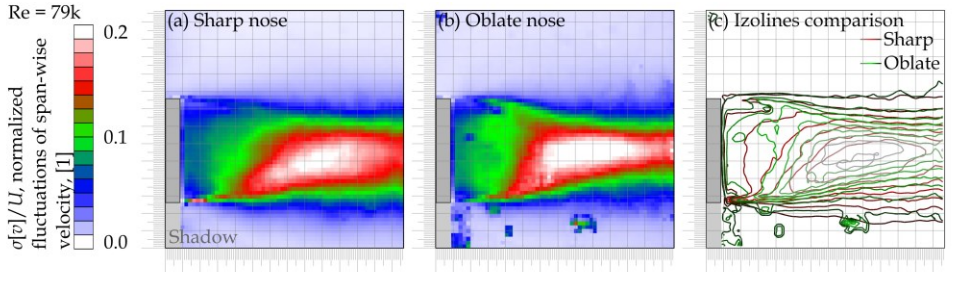

Fig. 19. Span-wise velocity fluctuations.

At the highest velocity and the case with oblate nose, we had severe troubles with the seeding particles. The measurement contains lot of noise caused by the presence of interrogation areas with too small number of particles. It is pity, because this velocity seems to show higher differences between the noses, especially in terms of wake width [42].

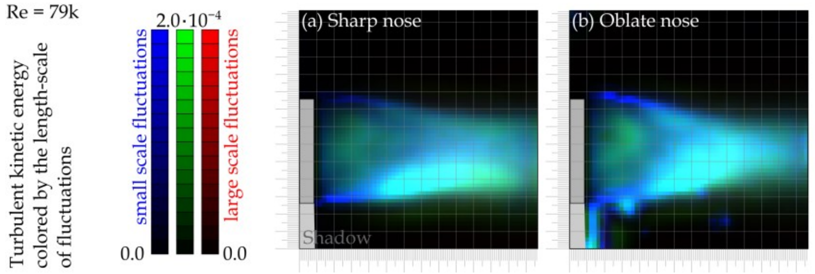

Fig. 20. Turbulent kinetic energy colored by the length-scale of fluctuations. Please read the articles [39] [8] [9] [9] for better understanding. Here, the blue colors represent small-scale fluctuations, green middle-scale and red large-scale.

5 Conclusion

We had a great opportunity to solve a small student project by using the amazing equipment of the University of West Bohemia in Pilsen. We asked a question inspired by the movie Dictator [1], if there is any difference between the rocket with oblate or sharp nose. We created a CAD model, we printed the parts, we checked the geometry by using optical scanning. Then we measured the subsonic flow at very low velocities of 5, 10 and 20 m/s in wind tunnel by using Particle Image Velocimetry (PIV [3]). We have made following observations:

1) The difference is small, but it increases with Reynolds number.
2) The wake of rocket with sharp nose heals faster.
3) Despite the careful model placement, there is an asymmetry.
4) The fluctuations in stream-wise or span-wise directions have very different topology. Stream-wise fluctuations peak at the boundary layers just behind the body, while the span-wise fluctuations reach their maximum value at the wake axis slightly behind the location of recirculation bubble.
5) The stream-wise fluctuations are associated with small-scale fluctuations, while the span-wise associate more with large-scale fluctuations.
6) It was very difficult to measure at velocity 20 m/s past the rocket with oblate nose.

The main goal of this work was to obtain the "zápočet" from the lecture "Člověk a energie". This goal has been successfully reached. The secondary goal is to attend the conference Power System Engineering and to present this work with hope for not too laud ridicule.

6 Acknowledgement

We thank very much to our amazing supervisor RNDr. Daniel Duda, Ph.D. Great thanks belong to Doc. Dr. Vitalii Yanovych, DrSc. for help with technical aspects of the measurement. We thank to professor Ing. Václav Uruba, CSc. We thank to our lecturer Ing. Martin Novák, Ph.D. for the preparation of these student projects. We thank to head officers of the Department of Power System Engineering for the possibility to attend the conference, namely to Ing. Pavel Žitek, Ph.D., doc. Ing. Václav Dostál, Ph.D., and to Michaela Vacková.

Reference

[1] L. Charles, Director, *The Dictator.* [Film]. United Kingdom, United States: Four By Two Films, 2012.

[2] G. Easanesan, D. Burton and M. C. Thompson, "The effects of nose-shape and upstream flow separation on the wake of a cylindrical square-backed body," *Experimental Thermal and Fluid Science,* vol. 118, p. 110142, 2020.

[3] R. J. Adrian, "Twenty years of particle image velocimetry," *Experiments in Fluids,* vol. 39, no. 2, pp. 159-169, 2005.

[4] S. R. Ahmed, G. Ramm and G. Faltin, "ome salient features of the time-averaged ground vehicle wake," *SAE Technical Paper Series,* vol. 93, pp. 473-503, 1984.

[5] M. Velmani and V. Suresh, "Numerical study of freestream turbulence effects on the nose cones in supersonic flow," *Aircraft Engineering and Aerospace Technology,* vol. 95, no. 2, pp. 214-224, 2023.

[6] D. A. Bountin, Y. V. Gromyko, P. A. Polivanov, A. A. Sidorenko, A. S. Nastobursky and A. A. Maslov, "Effects of temperature factor of cone nose-tip on a transition to turbulence," *AIP Conference Proceedings,* vol. 1770, p. 030061, 2016.

[7] X. D. Chen, T. H. Liu, X. S. Zhou, W. h. Li, T. Z. Xie and Z. W. Chen, "Analysis of the aerodynamic effects of different nose lengths on two trains intersecting in a tunnel at 350 km/h," *Tunnelling and Underground Space Technology,* vol. 66, pp. 77-90, 2017.

[8] D. Duda and V. Uruba, "PIV of air flow over a step and discussion of fluctuation decompositions," *AIP Conference Proceedings,* vol. 2000, p. 020005, 2018.

[9] A. Agrawal and A. Prasad, "Properties of vortices in the self-similar turbulent jet," *Experiments in Fluids,* vol. 33, p. 565–577, 2002.

[10] D. Duda, V. Yanovych, V. Uruba, V. Horáček, M. Němec, T. Jelínek, P. Žitek, V. Abrhám, P. Milčák, T. Kubíková, T. Tomášková and V. Tsymbalyuk, "Přehled některých výsledků laboratoře proudění na Západočeské univerzitě v Plzni od posledního sympózia v roce 2019," *Sympozium o Anemometrii 2022,* vol. 1, no. 1, pp. 1-14, 2022.

[11] S. Inkinen, M. Hakkarainen, A. Albertsson and A. Södergård, "From lactic acid to poly(lactic acid) (PLA): Characterization and analysis of PLA and Its precursors," *Biomacromolecules,* vol. 12, no. 3, pp. 523-532, 2011.

[12] S. Zhang, Handbook of 3D Machine Vision: Optical Metrology and Imaging, Boca Raton: CRC Press, 2013.

[13] D. Duda, V. Yanovych and V. Uruba, "An Experimental Study of Turbulent Mixing in Channel Flow Past a Grid," *Processes,* vol. 8, no. 11, p. 1355, 2021.

[14] D. Duda, V. Abrhám, V. Uruba and V. Yanovych, "Turbulent jet stability increased by ribs inside the nozzle – Stereo PIV measurement one diameter past the nozzle," *MATEC Web of Conferences,* vol. 345, p. 00006, 2021.

[15] V. Yanovych, D. Duda, V. Uruba and T. Tomášková, "Hot-Wire Investigation of Turbulence Topology behind Blades at Different Shape Qualities," *Processes,* vol. 10, no. 3, p. 522, 2022.

[16] D. Duda, V. Yanovych, V. Tsymbalyuk and V. Uruba, "Effect of Manufacturing Inaccuracies on the Wake Past Asymmetric Airfoil by PIV," *Energies,* vol. 15, no. 3, p. 1227, 2022.

[17] V. Yanovych, D. Duda, V. Horáček and V. Uruba, "Research of a wind tunnel parameters by means of cross-section analysis of air flow profiles," *AIP Conference Proceedings,* vol. 2189, p. 020024, 2019.

[18] V. Yanovych and D. Duda, "Using ARAMIS system for measurement of structural stability of running wind tunnel," *MATEC Web Conf.,* vol. 328, p. 01003, 2020.

[19] V. Yanovych, D. Duda, V. Uruba and P. Antoš, "Anisotropy of turbulent flow behind an asymmetric airfoil," *SN Applied Sciences,* vol. 3, p. 885, 2021.

[20] V. Yanovych and D. Duda, "Structural deformation of a running wind tunnel measured by optical scanning," *Strojnicky Casopis,* vol. 70, no. 2, pp. 181-196, 2020.

[21] C. Tropea, A. Yarin and J. Foss, Springer Handbook of Experimental Fluid Mechanics, Berlin: Springer, 2007.

[22] D. Duda, T. Jelínek, P. Milčák, M. Němec, V. Uruba, V. Yanovych and P. Žitek, "Experimental Investigation of the Unsteady Stator/Rotor Wake Characteristics Downstream of an Axial Air Turbine," *International Journal of Turbomachinery Propulsion and Power,* vol. 6, no. 3, p. 22, 2021.

[23] D. Duda, T. Jelínek, M. Němec, V. Uruba, V. Yanovych and P. Žitek, "Particle image velocimetry measurement inside axial air test turbine – Effect of window," *AIP Conference Proceedings,* vol. 2323, no. 1, p. 030005, 2021.

[24] D. Duda, J. Bém, V. Yanovych, P. Pavlíček and V. Uruba, "Secondary flow of second kind in a short channel observed by PIV," *European Journal of Mechanics, B/Fluids,* vol. 79, pp. 444-453, 2020.

[25] V. Uruba, P. Procházka, M. Sedlář, M. Komárek and D. Duda, "Experimental and Numerical Study on Vortical Structures and Their Dynamics in a Pump Sump," *Water,* vol. 14, no. 13, p. 2039, 2022.

[26] V. Uruba, D. Duda and V. Yanovych, "On Dynamics of Flow past a Stage Axial Air Turbine," *Journal of Physics: Conference Series,* vol. 2367, no. 1, p. 012023, 2022.

[27] M. La Mantia, D. Duda, M. Rotter and L. Skrbek, "Velocity statistics in quantum turbulence," *Procedia IUTAM,* vol. 9, pp. 79-85, 2013.

[28] P. Švančara, D. Duda, P. Hrubcová, M. Rotter, L. Skrbek, M. La Mantia, E. Durozoy, P. Diribarne, B. Rousset, M. Bourgoin and M. Gibert, "Ubiquity of particle-vortex interactions in turbulent counterflow of superfluid helium," *Journal of Fluid Mechanics,* vol. 911, p. A8, 2021.

[29] D. Duda, M. La Mantia and L. Skrbek, "Streaming flow due to a quartz tuning fork oscillating in normal and superfluid He 4," *Physical Review B,* vol. 96, no. 2, p. 024519, 2017.

[30] D. Duda, P. Švančara, M. La Mantia, M. Rotter and L. Skrbek, "Visualization of viscous and quantum flows of liquid He 4 due to an oscillating cylinder of rectangular cross section," *Physical Review B - Condensed Matter and Materials Physics,* vol. 92, no. 6, p. 064519, 2015.

[31] D. Duda, P. Švančara, M. La Mantia, M. Rotter, D. Schmoranzer, O. Kolosov and L. Skrbek, "Cavitation Bubbles Generated by Vibrating Quartz Tuning Fork in Liquid 4 He Close to the λ -Transition," *Journal of Low Temperature Physics,* vol. 187, no. 5-6, pp. 376-382, 2017.

[32] M. La Mantia, P. Švančara, D. Duda and L. Skrbek, "Small-scale universality of particle dynamics in quantum turbulence," *Physical Review B,* vol. 94, p. 184512, 2016.

[33] D. Duda, M. La Mantia, M. Rotter and L. Skrbek, "On the visualization of thermal counterflow of He II past a circular cylinder," *Journal of Low Temperature Physics,* vol. 175, no. 1-2, pp. 331-338, 2014.

[34] D. Duda, "Searching of Individual Vortices in Experimental Data," in *Vortex Dynamics - From Physical to Mathematical Aspects*, London, IntechOpen, 2022.

[35] D. Duda, V. Yanovych and V. Uruba, "Vortex profiles in grid turbulence observed by PIV," *AIP Conference Proceedings,* vol. 2672, p. 020002, 2023.

[36] T. von Kármán, Aerodynamics, McGraw-Hill paperbacks : science, mathematics and engineering ed., McGraw-Hill: McGraw-Hill, 1963.

[37] I. Solís-Gallego, A. Meana-Fernández, J. M. Fernández Oro, K. Argüelles Díaz and S. Velarde-Suárez, "Turbulence Structure around an Asymmetric High-Lift Airfoil for Different Incidence Angles," *Journal of Applied Fluid Mechanics,* vol. 10, no. 4, pp. 1013-1027, 2017.

[38] D. Duda, V. Yanovych, V. Horáček and V. Uruba, "Strouhal number and vortices in far wake of cylinder," *Journal of Physics: Conference Series,* vol. 2367, no. 1, p. 012017, 2022.

[39] D. Duda and V. Uruba, "Spatial spectrum from particle image velocimetry data," *Journal of Nuclear Engineering and Radiation Science,* vol. 5, no. 3, pp. 030912-1-030912-7, 2019.

[40] А. Н. Колмого́ров, "Локальная структура турбулентности в несжимаемой вязкой жидкости при очень больших числах Рейнольдса," *Воспроизводится по ДАН СССР,* vol. 30, p. 299, 1941.

[41] A. Agrawal, "Measurement of spectrum with particle image velocimetry," *Experiments in Fluids,* vol. 39, p. 836–840, 2005.

[42] D. Duda, V. Uruba and V. Yanovych, "Wake Width: Discussion of Several Methods How to Estimate It by Using Measured Experimental Data," *Energies,* vol. 14, no. 15, p. 4712, 2021.